Near real-time modelling of landslide impacts to inform rapid response: an example from the 2016 Kaikōura, New Zealand, earthquake

Tom R. Robinson[1], Nick J. Rosser[1], Tim R.H. Davies[2], Thomas M. Wilson[2], Caroline Orchiston[3]

[1]Department of Geography, Institute of Hazard, Risk & Resilience, Durham University, Durham, DH1 3LE, UK

[2]Department of Geological Sciences, University of Canterbury, Christchurch, 8041, New Zealand

[3]Centre for Sustainability, University of Otago, Dunedin, 9016, New Zealand

Correspondence to: Tom R. Robinson (tom.robinson@durham.ac.uk)

ABSTRACT

Reliable methods to undertake near real-time modelling of landslide hazard and associated impacts following an earthquake are required in order to provide crucial information to guide emergency response. Following the 2016 Kaikōura earthquake in New Zealand, we undertook such a near real-time modelling campaign in an attempt to pinpoint the location of landslides and identify where roads and rivers had been blocked. The model combined an empirical analysis of landslide hazard based on previously published global relationships with a simple runout model based on landslide reach angles. It was applied manually with a first iteration completed within 24 hours of the earthquake, and a second iteration, based on updated shaking outputs, within ~ 72 hours. Both models highlighted that landsliding was expected to be widespread and that impacts to roads were likely to mean Kaikōura township was cut-off. These results were used by

responders at the time to formulate aerial reconnaissance flight paths and to identify the risk of landslide dams causing further damage. Subsequent model verification based on available landslide inventories shows that while these models were able to capture a large percentage of landslides and landslide impacts, the outputs were over-predicted, limiting their use for pinpointing the precise locations of triggered landslides. To make future versions of the model more useful for informing emergency response, continued work to modify and adapt the approach to reduce this over-prediction is necessary. Nevertheless, the results from this study show the model is a promising initial attempt at near real-time landslide modelling and efforts to automate the approach would greatly increase the utility and speed of modelling in future earthquakes.

INTRODUCTION

Landsliding during earthquakes in mountain regions is a widespread hazard that has previously caused the majority of earthquake impacts to critical transport and utilities infrastructure (Bird & Bommer, 2004). Such impacts are important during emergency response as they can impinge access to affected regions, resulting in delays in search and rescue activities and the delivery of aid. As well as obstructing infrastructure networks, landslides falling into rivers can emplace landslide dams that block the river and cause upstream flooding. Catastrophic failure of these dams can result in an outburst flood that can devastate downstream communities. Landslide dams that fail typically do so soon after formation, with 41% of those that eventually fail, failing within one week (Costa & Schuster, 1988). Pinpointing the locations where landslides block transport routes and rivers post-earthquake in near real-time is therefore an important goal for informing emergency response.

While a number of near real-time models of earthquake processes such as ground shaking and resulting fatalities have been successfully developed (e.g. Jaiswal et al., 2009; Trendafiloski et al., 2011), relatively little research has focussed on near real-time modelling of coseismic landslides. Several recent methods have been attempted based either on a simplified Newmark analysis (Jibson et al., 2000; Godt et al., 2008; 2009; Gallen et al., 2016) or using an empirical approach (Nowicki et al., 2014; Kritikos et al., 2015; Robinson et al., 2017), but none are currently operational and very few have been applied during a live earthquake response. Approaches based on a simplified Newmark analysis combine information on ground shaking, slope angle, and local material strength to assess the resulting slope deformation (Newmark, 1965). However, local material strength properties are rarely known, especially at scales relevant to landslides, necessitating assumptions on rock strength and its variability, which can lead to widely varying model outputs (Dreyfus et al., 2013; Gallen et al., 2016). These assumptions can only be tested following the completion of event-specific landslide inventories, which can take many months to complete (Williams et al., 2017).

Approaches using empirical analysis rely on observations of previous coseismic landslides to ascertain the relationships between various predisposing factors and landslide occurrence. Such models assume that the characteristics of locations where landslides have previously been observed are representative of those where future landslides will occur. Typically this approach has only been applied to a specific location; however, recent approaches have attempted to use observations from multiple different locations to establish global relationships (Nowicki et al., 2014; Kritikos et al., 2015; Marc et al., 2016; Parker et al., 2017). However, in order to produce global relationships, such methods cannot consider local factors like lithology or soil characteristics which are known to limit the accuracy of landslide models in

specific cases (Bozzano et al., 2008). Further uncertainties arise from studies that have shown seasonal variations in slope failures during earthquakes (Chousianitis et al., 2016) that are also not included in global relationships.

In this study, we describe a near real-time coseismic landslide modelling campaign undertaken following the 2016 Kaikōura earthquake in New Zealand. This landslide hazard modelling used an empirical approach based on adapted global relationships from Kritikos et al. (2015). However, unlike previous attempts, our modelling also incorporated an analysis of the risk landslides posed to major roads and rivers in the affected area using a simplified assessment of potential reach angles. The results of these models were shared at the time with emergency managers and science responders on the ground. Here, we describe the methods and results of this near real-time modelling campaign along with quantitative analyses of model performance based on available data. We discuss the rapidity with which this modelling was undertaken as well as the resulting accuracy, and highlight the relative strengths and weaknesses of the approach taken. Necessary improvements to further reduce the modelling time and increase the model accuracy and utility are also discussed along with the potential to automate the method as an add-on to other already available rapid earthquake modelling tools.

SETTING

Earthquake and landslide hazard

The Kaikōura earthquake occurred at 11:02 hrs on 13 November 2016 UTC (Coordinated Universal Time) at a depth of 15 km and had a magnitude of M_w 7.8 (Fig. 1). The event propagated northward for > 170 km in a complex rupture involving multiple previously known and unknown faults (Hamling et al., 2017), making it one of the most complex earthquakes ever

recorded. Strong ground shaking of up to MMI IX was recorded along the entire rupture length and consequently at least 10,000 landslides are thought to have occurred (Kaiser et al., 2017; Dellow et al., 2017; Massey et al., This Issue). Along with fault surface rupture, landslides caused extensive damage to transport infrastructure in the affected area (Fig. 1), in particular to State Highway (SH) 1 and the Inland Kaikōura Road (Stirling et al., 2017; Davies et al., 2017). This resulted in the isolation of Kaikōura township along with a number of other rural communities in North Canterbury and southern Marlborough, leading to emergency air and sea evacuations of > 600 stranded tourists (Davies et al., 2017). Road access to Blenheim and Picton from Christchurch remained possible, but only via a > 200 km detour through steep mountain passes (Fig. 1), adding over 7 hours to journey times. As well as damage to lifelines, > 190 landslide dams were formed (Fig. 1) throughout the affected area (Dellow et al., 2017). The majority of these occurred in steep but small river catchments and consequently presented little risk to local populations; however, at least 11 landslide dams were judged by regional Civil Defence and Emergency Management (CDEM) groups to present a severe risk to downstream populations and infrastructure.

Transport infrastructure

The region is steep and mountainous, rising from sea-level to over 2,500 m in ~ 20 km, with the mountain ranges ending at the coast in steep cliffs. Despite this, the region is an important transport corridor, particularly for freight and tourism. SH1 is the main arterial road access between Christchurch and the tourist destinations of Kaikōura and Blenheim, traversing a narrow corridor between the coast and mountains for > 100 km between Oaro and Ward (Fig. 1). Alternative access between Christchurch and Kaikōura is possible via the Inland Kaikōura Road (IKR), which passes through less steep terrain and connects to SH7, however no alternative road

112 access exists between Kaikōura and Blenheim. An alternative route between Christchurch and
113 Blenheim via SH7 adds an additional 200 km to the journey and passes through steep alpine
114 terrain (Fig. 1), making it unfavourable for heavy goods vehicles. This route is also vulnerable to
115 alpine hazards (Robinson et al., 2015) highlighting the lack of redundancy in the South Island
116 road network. The only other routes providing north-south access in this region are the Awatere
117 Valley Road and the Wairau-Hanmer Road, both of which are suitable for 4x4 vehicles only and
118 therefore provide emergency access only.

119 **Previous landslide impacts**

120 Given the mountainous nature of the South Island, temporary road closures due to landslides are
121 not uncommon, especially after earthquakes. A series of moderate earthquakes in 1994 caused
122 substantial damage to SH73, which is one of only three routes east-west across the Southern
123 Alps, closing the road for several days and restricting traffic for over one week (Paterson &
124 Bourne-Webb, 1994). Following the 2003 M_w 7.3 Fiordland earthquake, landslides caused minor
125 damage to several roads including SH94, which provides the only road access to Milford Sound
126 (Power et al., 2005). Most of these blockages resulted from small rockfalls and debris flows and
127 consequently were quickly cleared. The most extensive recent impacts to roads from landslides
128 were caused by the 2010-11 Canterbury earthquake sequence, which caused widespread damage
129 throughout the city of Christchurch (Bannister & Gledhill, 2012). Substantial rockfalls in the
130 Port Hills resulted in several road closures (Giovinazzi et al., 2011).

131 Landslide dams are common in New Zealand due to a combination of steep terrain,
132 narrow valleys, and high seismicity and rainfall. At least 232 landslide dams have been
133 documented, of which 39% are thought to have resulted from earthquakes, although the trigger
134 for a further 59% remains unexplained (Korup, 2004). While data on dam failures is thought to

be under-reported, Korup (2004) assessed the time to failure for those that did fail and suggested that minimum decision-making times varied with dam volume, ranging from several minutes to several days as volume increased. Generally, New Zealand was found to have larger volume dams and impounded lakes than other mountainous regions.

DATA & METHODS

Landslide hazard modelling

The model employed following the Kaikōura earthquake was based on the empirical analysis established by Kritikos et al. (2015). Their approach used fuzzy logic in GIS to combine the effect of multiple predisposing factors, with the corresponding functions derived from observations of the 1994 Northridge, 1999 Chi-Chi, and 2008 Wenchuan earthquakes. Robinson et al. (2016a) later showed that the same functions also accurately modelled landslide hazard from the 2003 and 2009 Fiordland earthquakes in southern New Zealand, confirming that the approach was applicable more widely. Fuzzy logic-based approaches to landslide modelling have previously been shown to match or out-perform other approaches (Pradhan, 2010; Bui et al., 2012; Pourghasemi et al., 2012). However, most importantly for near real-time modelling, these approaches are fast to apply, as much of the necessary input data can be derived and stored pre-event (Fig. 2), reducing the amount of data collection required following an earthquake.

Fuzzy logic

Fuzzy logic considers the role of multiple different factors influencing landslide occurrence, and models how these different factors combine simultaneously to cause landslides from a specific earthquake. Each predisposing factor is assigned a membership function, $\mu(x)$, that describes the

156 factor's relationship with landslide occurrence (e.g. increasing landslide frequency with
157 increasing slope angle) based on previous observations. These membership functions take values
158 [0, 1] where 0 represents the value of a given factor with the lowest frequency of landsliding, and
159 1 represents the highest frequency of landsliding. Each predisposing factor is therefore converted
160 into a fuzzy factor that effectively describes where landslides are more or less likely to occur as a
161 result of that individual factor. These fuzzy factors are then combined on a pixel-by-pixel basis
162 to establish the likelihood of landslides occurring in any given pixel from the specific earthquake
163 (i.e. landslide hazard). This combination of factors is a critical step in the process and
164 consequently various different combination approaches exist. However, for physical phenomena
165 such as landslides, the fuzzy gamma operator has been shown to be the most appropriate method
166 (Pradhan, 2010; Bui et al., 2012; Kritikos et al., 2015). Fuzzy gamma combines multiple factors
167 such that:
168
169 $$L_{HZ} = \left[\prod_{F=1}^{j} \mu(x)\right]^{1-\gamma} \cdot \left[1 - \prod_{F=1}^{j} 1 - \mu(x)\right]^{\gamma} \quad (1)$$
170
171 where L_{HZ} represents landslide hazard, $\mu(x)$ is the membership function for factor F, j is the
172 number of factors to be combined, and γ is a constant. The value of γ strongly affects the output
173 L_{HZ} values, with Kritikos & Davies (2015) showing that the optimum value for landslide hazard
174 analysis was 0.9; smaller values consistently under-predicted landslide occurrence, while larger
175 values consistently over-predicted.

Hazard model parameters and data inputs

The model requires inputs of local slope angle (*SA*), Modified Mercalli Intensity (*MMI*), slope position (*SP*), fault proximity (*FD*), and river proximity (*RD*). Local slope angle, slope position, and river proximity can all be readily obtained from a GDEM. Fault maps are available either from local geologic agencies or from the global earthquake model (GEM) active fault database, and *MMI* distribution can be calculated from a combination of ground motion prediction equations, felt reports, and instrumental data within minutes of an earthquake occurring (Wald et al., 2008; Horspool et al., 2015). We used the open-source Land Information New Zealand (LINZ) national DEM (~ 25 m horizontal resolution) to calculate local slope angle and slope position, as well as the LINZ river network to define river proximity. Fault locations were taken from the GNS Science active fault database, which, at the time, did not include several of the faults involved in the earthquake (Hamling et al., 2017; Stirling et al., 2017). *MMI* was taken from two different sources: USGS ShakeMap®, and GeoNet earthquake records. This allowed two versions of the model to be produced in near real-time, facilitating comparison between the outputs to provide a degree of confidence around the results. The fact that several faults involved in the rupture were not included in the active fault map available at the time is important, as many landslides were subsequently found to have occurred very near to, or directly on these fault ruptures (Massey et al., This Issue). Further, the initial USGS ShakeMap output that was used did not account for such a complex rupture, instead basing shaking estimates on simple ground motion prediction equations (GMPEs).

The membership functions for each factor used in this study are (Kritikos et al., 2015):

$$\mu(SA) = \begin{cases} 0, SA \leq 15° \\ 1/1 + (SA/4.875)^{-2.65}, SA > 15° \end{cases} \quad (2)$$

$$\mu(MMI) = 1/1 + (MMI/7.5)^{-14} \quad (3)$$

$$\mu(FD) = 1/1 + (FD/2.375)^{5.375} \quad (4)$$

$$\mu(RD) = 1/1 + (RD/3.25)^{5.5} \quad (5)$$

$$\mu(SP) = 1/1 + (SP/2.325)^{-4.375} \quad (6)$$

Following the method of Kritikos et al. (2015), each factor was classified into different bins numbered consecutively from smallest to largest, with the bin number forming the input variable for the corresponding membership function (Table 1). We adapted the original membership function for slope angle to force slopes ≤ 15° (bins 1-3) to have $\mu(x) = 0$, assuming no landslides will occur on these slopes. A simplified work flow showing the various input parameters and model steps is shown in Figure 2.

Impact modelling

Danger pixels and landslide reach angle

Modelling impacts resulting from landslides is a complex task due to difficulties in predicting landslide runout paths, amongst other factors. Several attempts have used an approach based on danger pixels, which identify the locations where impacts are likely based on the intersection between landslide hazard pixels and infrastructure pixels (Kanungo et al., 2008; Pellicani et al., 2014). These models typically use a semi-quantitative approach whereby landslide hazard is classified into zones of low, medium, high etc. with only the highest zones classified as danger pixels. Other attempts have focussed on using a simple horizon scanning approach to identify

219 network viewsheds in order to directly assess the risk to pre-existing and planned networks
220 (Robinson et al., 2016b), or to plan least-cost landslide-safe routes for new networks (Meinhardt
221 et al., 2015). However, in these approaches, all pixels within the viewshed are effectively
222 considered as danger pixels, irrespective of their corresponding landslide hazard or the reach
223 angle to the network concerned.

224 The reach angle, θ, of a landslide is an important measure of landslide mobility (Hsü,
225 1975; Hungr, 2006) and is derived from the angle of a line connecting the top of the landslide
226 scar to the distal toe of the deposit (Fig. 3). Calculating the reach angle between a specific
227 segment of a road/river network and the pixels within the corresponding viewshed therefore
228 identifies the relative mobility required for landslides in those viewshed pixels to intersect the
229 network segment (Fig. 3). Setting a minimum threshold reach angle that represents the largest
230 expected landslide mobility therefore identifies those pixels from which any landslide is
231 expected to have sufficient mobility to reach the network, i.e. the danger pixels, and eliminates
232 those pixels from which mobility is expected to be insufficient. The modelled landslide hazard
233 values within the corresponding danger pixels represent the likelihood of a landslide occurring,
234 and thus we therefore calculate the blockage risk based on the average modelled hazard values of
235 the danger pixels within a given network segment's corresponding viewshed. This ensures that
236 the only pixels contributing to the blockage risk calculation a) have runout directions broadly
237 towards the network; and b) have reach angles that suggest any landslide(s) will have sufficient
238 mobility to reach the network. This approach therefore improves upon previous approaches by
239 considering the potential mobility of landslides that occur as well as facilitating a fully
240 quantitative approach.

241 A key component of this approach is establishing the threshold reach angle. Several
242 studies have suggested that landslide reach angles are rarely < 30° (Hungr, 2006; Borella et al.,
243 2016); however, landslides with large volumes (> 10^6 m^3) or flow-type mechanisms have been
244 shown to commonly have reach angles < 30° (Davies et al., 1999; Hungr, 1995; Legros, 2002),
245 with several examples of reach angles < 5° (e.g.Wadge et al., 1995). For the near real-time
246 modelling undertaken following the Kaikōura earthquake, a minimum threshold angle of 30° was
247 used; however, after the event, once data on landslide locations and impacts became available, a
248 sensitivity analysis of the effect of changing this threshold angle was performed.

249 ***Loss model parameters and data inputs***

250 Calculating θ for each pixel in a viewshed with respect to a given segment of a network is a
251 simple task that can be undertaken rapidly. It requires comparing the elevation difference, H, and
252 the horizontal distance, L, between the network segment and each pixel in the corresponding
253 viewshed (Figs. 2 & 3) such that:
254
255 $$\theta = \tan^{-1} {}^{H}/_{L} \quad (7)$$
256
257 No measure of network vulnerability to landslides was included in the near real-time
258 analysis, with the results consequently only representing the likelihood of landslides reaching
259 and presumably obstructing the network. While vulnerability information may be important for
260 restoration estimates, longer term recovery planning, and estimating economic losses (Robinson
261 et al., 2015), at the time this analysis was undertaken it was thought the most pressing

information related to network obstruction. Nevertheless, future analyses may be able to account for vulnerability.

Road and river centrelines were downloaded from the LINZ open-source data repository and the horizontal distance from each network was calculated using the Euclidean Distance tool in ESRI's ArcGIS. Only order 3 and above rivers were evaluated as a) the total number of order 1 and 2 rivers is extremely large and thus increases the total time required to complete modelling; and b) landslide dams occurring on order 1 and 2 rivers were at the time considered unlikely to present a substantial hazard due to the limited catchment size. The road network was filtered to only include State Highways and other primary and emergency access roads, including the Awatere Valley Road and the Wairau-Hanmer Road (Fig. 1). To reduce modelling time, both networks were split into 1 km segments with danger pixels calculated for the mid-point of each segment. This was thought to provide the best compromise between modelling speed and useful output resolution. This resulted in 1,832 road segments and 8,456 river segments.

Model application and distribution

At the time of the Kaikōura earthquake, efforts to test, automate, and operationalise the model (Fig. 2) were underway but had not yet been completed. However, the relative simplicity of the approach combined with the availability of data allowed the modelling to be undertaken manually. Modelling was undertaken remotely in the UTC time zone (13 hours behind New Zealand Standard Time, NZST, at the time) on a single workstation using ESRI's ArcGIS.

The model results were made available to the New Zealand Science Advisory Group (SAG), which was tasked with aiding both the scientific and emergency responses to the earthquake and comprised various scientists from New Zealand's Universities and GNS Science amongst others (Woods et al., 2017). Results were initially uploaded to a closed access

geospatial portal (*Engineering Response to the M7.8 Kaikōura earthquake clearinghouse*, henceforth referred to as the clearinghouse, see Data and Resources Section) to enable data sharing between members. This was accessible only to members of the SAG, allowing model results to be independently reviewed and discussed before being shared openly with relevant stakeholders and the public. While delaying the public distribution of model results, this allowed crucial discussions on the model's potential accuracy and utility, which was felt necessary due to this being the first event the model had been applied to in near real-time. It also facilitated discussions as to which stakeholders would benefit most from the model outputs. A more detailed discussion of the distribution and utility of model results is provided below.

RESULTS

Model 1: 0 days 21 hours 28 minutes post-earthquake

Within a few hours of the earthquake occurring, consideration was given to whether manual application of the model could produce results quickly enough to be of use in the response. These discussions were hampered by the earthquake occurring on a Sunday in the UTC time zone (Monday morning in NZST); however, approximately 18 hours after the earthquake occurred, it was decided that manual application of the model could still be undertaken within a useful timeframe. Manual downloading and processing of the necessary data sets began at approximately 06:00 hrs on 14 November UTC, 0 days 18 hrs 58 mins after the earthquake occurred. Priority was given to the largest datasets, namely the LINZ DEM and rivers database, which required the longest downloading and processing times. Shaking data at this time were sourced from the USGS ShakeMap® (see Data and Resources Section), which released initial models < 10 mins after the earthquake based on GMPEs, and at the time was the only openly

307 available shaking data for the event. Data collection and processing were completed at 07:59 hrs
308 on 14 November UTC, 0 days 20 hrs 57 mins after the earthquake occurred. Model 1 (Fig. 4)
309 was subsequently completed and data provided to the SAG at 08:30 hrs on 14 November UTC, 0
310 days 21 hrs 28 mins after the earthquake occurred. Model 1 was therefore completed
311 approximately 2 hrs 30 mins after data collection and processing began, and just 31 mins after
312 this procedure was completed.

313 According to Model 1, the highest probability of landslides was concentrated in two
314 coastal areas immediately north and south of Kaikōura, where landslide likelihoods exceeded
315 80%. By this time several social media posts had reported landslides near to Kaikōura with
316 reports of blockages on SH1, but the full extent and intensity of landsliding was not yet known.
317 Landslide likelihoods > 60% (referred to as high risk i.e. those pixels where landslides were
318 more likely to occur than not) were modelled extending northwards from Waiau to Blenheim (~
319 130 km) and stretching inland from the coast for ~ 50 km to the slopes east of the Awatere
320 Valley Road, affecting a total area of ~ 6,500 km^2, suggesting that landsliding was expected to be
321 widespread.

322 Of the 1,832 road segments modelled, 560 (~ 30%) were identified as having at least one
323 danger pixel (i.e. with $\theta \geq 30°$); the remaining 1,272 segments have no danger pixels andwere
324 therefore considered to have no risk of landslide blockage. The most at-risk road segment was
325 located 20 km north of Kaikōura on SH1 at a location known as Ohau Point, where the risk of
326 blockage was 75%. In total, 46 segments of road were considered high risk (> 60%), of which 38
327 were on SH1 and three on the IKR. This immediately highlighted the possibility that Kaikōura
328 might be isolated with no road access possible. In addition, two segments on SH7 south of

Hanmer Springs were identified as high risk, along with three segments on the Awatere Valley Road.

Out of the 8,456 river segments modelled, 5,089 were identified as having at least one danger pixel, emphasising the high potential for landslide dam formation in this part of New Zealand. In total, 241 river segments between Waiau and Blenheim, and stretching inland as far as the Awatere Valley Road, achieved high modelled risk values, suggesting that numerous landslide dams were to be expected throughout this region. The highest likelihood was 79% and occurred ~ 40km north-east of Kaikōura on the Clarence River. At the time, a landslide dam was known to have occurred and subsequently failed at approximately 03:00 hrs on 14 November UTC (Dellow et al., 2017), ~ 16 hrs after the earthquake and ~ 5 hrs 30 mins before Model 1 was completed. While Model 1 was not completed in time to identify the Clarence River dam, this provided confidence in the model's ability to produce useful results for other rivers.

Model 2: 3 days 1 hour 28 minutes post-earthquake

Following the completion of Model 1, we became aware that an alternative shaking model based on local strong motion data sensors (see Horspool et al., 2015) had been released by GeoNet (see Data and Resources Section), a collaboration between the New Zealand Earthquake Commission and GNS Science that records information on New Zealand hazards. This data was downloaded at 10:12 hrs on 16 November UTC, 2 days 23 hrs 10 mins after the earthquake; however, these data were available at least as early as 22:06 hrs on 15 November UTC. Consequently, a second round of landslide modelling based on this data was undertaken. Model 2 (Fig. 5) was completed and shared with the SAG at 12:30 hrs on 16 November UTC, 3 days 1 hr 28 mins after the earthquake occurred. Combining these results with Model 1 at the time allowed the authors and

351 the SAG to qualitatively evaluate the level of (un)certainty to place on the outputs, allowing
352 varying degrees of confidence to be placed on the resulting conclusions.

353 In total, 60% of pixels, accounting for an area ~ 19,000 km^2, were unchanged in terms of
354 landslide hazard between Model 1 and Model 2. A total of 17% of pixels (~ 5,500 km^2) increased
355 in hazard, although of these, 75% increased by ≤ 10%, a change that was considered negligible.
356 Significant hazard increases therefore occurred in just 4% of pixels (220 km^2), the majority of
357 which were located on the eastern-most slopes between Kaikōura and Ward, but some of which
358 were on slopes south of Waiau (Fig. 5). However, there were also significant hazard decreases
359 (changes > 10%) on slopes east of the Awatere Valley Road. Consequently, high landslide
360 hazard values (> 60%) in Model 2 extended north-east along the coast for ~ 170 km and inland
361 for ~ 40 km, affecting a total area of ~ 6,800 km^2, which is slightly larger than Model 1. The
362 maximum modelled landslide hazard increased from 85% to 89% but remained in the same area
363 as Model 1, on the slopes immediately north of Kaikoura (Fig. 5b).

364 Notwithstanding the slight increase in some landslide hazard values in Model 2, there
365 was little overall change in the total modelled risk of road blockages. In total, risk values
366 increased for 44 road segments, with an average increase of 6%, and decreased for 37 segments,
367 with an average decrease of 7%. Notably, the highest risk of blockage on the network remained
368 on SH1 at Ohau Point, where it increased to 76%. The total number of road segments considered
369 high risk increased from 44 in Model 1 to 62 in Model 2, with 15 of these located on SH1 south
370 of Oaro and one each for SH7, the IKR, and the Awatere Valley Road. Despite this, there was a
371 notable decrease in risk values for several segments of SH1 north and south of Kaikōura, where
372 risk decreased from ~ 65% to < 20% (Fig. 5c).

373 Very little change in terms of landslide dam risk was observed between Model 1 and
374 Model 2, with 4,341 river segments (85% of the 5,089 at-risk segments) having scores that
375 differed by < 10% from Model 1. Of the 748 segments that changed by > 10%, 266 increased in
376 Model 2, 184 of which were located east of the Awatere Valley Road. The effect was to increase
377 the total number of river segments considered to be at high risk of blockage from 241 in Model 1
378 to 314 in Model 2. The majority of these changes occurred on rivers south of Waiau in the region
379 where landslide hazard also notably increased in Model 2 (Fig. 5b). The risk of landslide dams in
380 this region changed from 50-60% in Model 1 to 60-70% in Model 2. Consequently, Model 2
381 suggested that numerous landslide dams were expected to have occurred in this region,
382 something which Model 1 had not necessarily highlighted. The highest modelled risk was again
383 on the Clarence River, where risk increased marginally to 80%.

384 **MODEL VERIFICATION AND SENSITIVITY**

385 Quantitative analysis of the model's predictive ability in terms of landslide hazard, road blockage
386 risk, and landslide dam risk is undertaken by comparing the corresponding true and false positive
387 prediction rates. True positive rate, or hit rate, is the number of observed landslides (or
388 blockages) occurring in pixels predicted as a landslide as a percentage of the total number of
389 observed landslides. False positive rate, or false alarm rate, is the total number of pixels
390 predicting a landslide that have landslide non-occurrence as a percentage of the total number of
391 non-occurrence pixels. Because this requires the landslide hazard and risk results to take the
392 form of a binary prediction (i.e. landslide or no landslide; blocked or not blocked) rather than
393 continuous values, we set various threshold hazard and risk values in which pixels/segments
394 above the threshold predict landslide occurrence/blockage. We compute the number of hits and

false alarms for multiple hazard and risk thresholds taken at 0.01 intervals in order to test how the predictions vary with increasing values of hazard and risk. Data on mapped landslides, road blockages, and landslide dams is taken from a variety of publically available sources or through the clearinghouse (see Data and Resources Section).

As well as the hit rate and false alarm rate, we calculate the relative true positive (RTP) rate. This considers the proportion of hits as a proportion of all pixels predicting landslide occurrence. A relative true positive rate of 75% therefore means three-quarters of all pixels predicting landslides are hits, regardless of the absolute number of hits this represents. This provides a measure of how much over-prediction is occurring in the model.

Landslide hazard models

For landslide hazard (Figs 4b & 5b), we use a dataset of 10,454 landslide centroid points (Fig. 1) mapped by GNS Science from satellite and aerial reconnaissance in the months following the earthquake (Massey et al,. This Issue). From this inventory, both models have a maximum hit rate of 81% (Fig 6a), meaning that 19% of mapped landslides occurred in pixels where landslide hazard = 0, i.e. slopes < 15°. This suggests this threshold may be too high for this event. The maximum false alarm rate is similar for both models at a little over 50%. Importantly, the number of false alarms decreases rapidly once hazard thresholds exceed 20% likelihood, while the number of hits remains close to the maximum until hazard thresholds reach ~ 50% likelihood. For thresholds > 50%, Model 2 notably achieves more hits than Model 1 for the same threshold value (Fig. 6a); for high hazard pixels (likelihoods > 60%), Model 1 predicts 47% of mapped landslides while Model 2 predicts 62%. This suggests that Model 2 forms the better overall prediction, but that broadly both results are comparable.

Nevertheless, the RTP rates for both models are very low: Model 1 has a maximum RTP rate of 9% while Model 2 has a maximum RTP rate of 22% (Fig. 6a). This means that both models severely over-predict landslide hazard with ~ 80-90% of pixels where landslides were predicted not experiencing a landslide. One reason for such low RTP rates is the large number of non-occurrence pixels (>10^7). Thus a false alarm rate of 2-6% equates to a large number of individual pixels compared to the number of observed landslides. However, it should be highlighted that the landslide inventory used to calculate RTP rate is point source and therefore each landslide is only represented by a single pixel. In reality, each landslide likely covers multiple pixels which in the present analysis are considered non-occurrence pixels; Massey et al. (This Issue) show that the mean landslide area is ~ 300 m^2, which equates to 12 pixels with a 25 m pixel size, while the largest was ~ 1,000,000 m^2, or 40,000 pixels. Consequently, the RTP rates are minimum estimates and in reality, the model likely performs better than these values suggest. Nevertheless, it is still likely that the results are over-predicted in terms of individual pixels. This issue is common to most landslide hazard and susceptibility models and reflects the difficulties associated with predicting landslide occurrence at such fine resolution.

Landslide road blockage risk models

Road blockage risk predictions are tested using the 41 road blockages (Fig. 1) reported by the New Zealand Transport Agency (NZTA). The approximate locations of many of these blockages were known within a few days of the earthquake from a combination of aerial reconnaissance and local reports. However, an official inventory with precise coordinates was not available on the clearinghouse until > 1 week after the earthquake. Because risk was calculated for 1 km segments of the road network, we compare observed blockages to the corresponding road segment, and consequently some road segments may account for multiple observed blockages.

Model 1 achieves a maximum hit rate of 93% while Model 2 achieves 98%, with both models achieving a maximum false alarm rate of 29% (Fig. 6b). However, there is a notable disparity between the number of hits achieved as the risk values increase (Fig. 6b). Model 1 sees no reduction in the number of hits until the risk threshold exceeds 53%, while Model 2 sees decreases once the risk threshold exceeds 20%. For high risk segments, Model 1 successfully predicts 71% of road blockages compared with Model 2 which predicts just 34%. Despite differences in the decay in number of hits, both models have a similar decay in false alarms, with virtually no false alarms registered in high risk segments.

Unlike with the raw hazard models, Model 1 is able to achieve high RTP rates, suggesting the model works well as a predictive tool. A blockage risk threshold set at 60% likelihood successfully predicts 70% (29 out of 41) of road blockages with an RTP rate of 66%, which increases to 100% when the blockage risk threshold is increased to 68% likelihood (Fig. 6b). Comparatively, at a 60% blockage risk threshold, Model 2 achieves an RTP rate of just 23% and accounts for just 34% of all observed blockages. Model 1 therefore not only forms the better predictive model for road blockages, but it is useful for pinpointing the precise road segments blocked by landslides with comparatively small over-prediction compared to the raw hazard model. Nevertheless, the failure of Model 2 is surprising given it formed a marginally better hazard prediction compared to Model 1.

Landslide dam risk models

Landslide dam predictions are tested using a dataset of 58 landslide dams (Fig. 1) mapped by GNS Science and others from aerial and ground-based reconnaissance, which was first publically available from Environment Canterbury (see Data and Resources Section) on 1 December 2016 UTC (18 days after the earthquake). In total, Dellow et al. (2017) describe > 200 landslide dams

463 while the Environment Canterbury dataset contains 191; however, the majority of these are
464 located on order 1 and 2 rivers, which were not assessed in the near real-time modelling
465 campaign. Consequently, only the 58 landslide dams (30% of the total identified) located on
466 order 3 or larger rivers are used to quantitatively assess model performance. This suggests that
467 the modelling should have considered order 1 and 2 rivers as this is where the majority of
468 landslide dams formed and, in hindsight, river order is not directly attributable to consequent
469 landslide dam risk. As with road blockages, we compare observed landslide dams to the
470 corresponding river segment, and individual segments may therefore account for multiple
471 blockages.

472 Both models achieve maximum hit rates of 93%, with Model 2 accounting for 90% of
473 landslide dams in high blockage risk segments (Fig. 6c). However, both models have high
474 maximum false alarm rates, with Model 1 having 60% and Model 2 having 59%. Nevertheless, a
475 similar decay pattern is observed, with the number of false alarms decreasing for both models
476 when blockage risk thresholds exceed 15% while the number of hits remains constant until
477 blockage risk thresholds exceed 50%. Notably, Model 2 does not see hit rates decrease until
478 blockage risk thresholds exceed ~ 60% at which point the decay rate is similar to Model 1,
479 suggesting Model 2 is the better version.

480 RTP rates for landslide dam predictions are notably lower than achieved for road
481 blockage predictions and only marginally better than the low scores observed for the raw hazard
482 models. Model 1 achieves a maximum RTP rate of just 14%, while Model 2 achieves a
483 maximum of 29% (Fig. 6c). Again, this highlights that both models over-predict landslide dam
484 risk and, currently, may not be useful for pinpointing the exact locations of landslide dams. Part
485 of this issue may lie in the threshold reach angle used (30°) as in reality the total landslide

volume passing this threshold may be insufficient to dam a river. Nevertheless, the high hit rates are encouraging, and if future iterations of the model can sustain such hit rates while reducing the over-prediction, this model may form a useful tool for pinpointing landslide dam locations.

Sensitivity analysis

Using the output landslide hazard from Model 1, we now reassess the road blockage and landslide dam risk using reach angle thresholds between 10° and 50° taken at 10° intervals, and compare the number of hits and false alarms achieved with the results achieved during the modelling campaign. The area between the true and false positive curves is calculated to find the best performing model. For this analysis we use the outputs from Model 1 as this version achieved comparable predictions for landslide dams and better predictions for road blockages compared to Model 2.

For both road blockages and landslide dams, smaller reach angle thresholds are able to achieve greater maximum hit rates (Fig. 7). The decay in hit rates with increasing risk values is broadly equivalent for all thresholds however. Smaller threshold reach angles also achieve greater false positive predictions (Fig. 7). The best performing threshold for road blockages is found to be 30°, although the performance using 20° and 40° is comparable (Table 2). For landslide dam risk, the 40° threshold achieves the greatest performance, although again the performance of the 20° and 30° thresholds are comparable. We also calculated the RTP rates for each of these thresholds, finding that for landslide dams the 40° threshold achieved a maximum RTP rate of 25%, approximately double that of the 30° threshold (14%). Whilst still too low to be useful for pinpointing landslide dams, this does suggest that if a similar increase were observed for a 40° threshold in Model 2 (translating to a maximum RTP rate of ~60%), then this version would begin to be useful for pinpointing landslide dams. This suggests that in future

applications of the model using a 40° reach angle threshold may be more appropriate for landslide dam prediction, while retaining a 30° reach angle threshold for road blockages is suitable. This likely relates to the landslide volume passing the corresponding reach angle; comparatively little landslide debris is required to block traffic flow on roads compared to that required to block river flow.

DISCUSSION

Model 2 road blockage risk

It is notable that Model 2 performs poorly at predicting road segments blocked by landslides, despite performing marginally better than Model 1 at predicting landslide hazard and landslide dam occurrence. The reason for this poor performance is Model 2's failure to successfully predict 19 (46% of the total) road blockages on SH1 near to Kaikōura that were successfully predicted by Model 1. Analysis of the mechanism causing this highlights that this failure resulted from an error during the processing of the GeoNet shaking model during the near real-time modelling campaign.

The GeoNet data does not provide offshore locations with *MMI* values (Fig. 5a). Shaking data from GeoNet was downloaded as a gridded XML format, which contains point locations with *MMI* values spaced at 1 km intervals; any points offshore are nominally assigned *MMI* = 1. To convert a gridded point cloud into a raster file necessary for the landslide hazard modelling, an inverse distance weighted interpolation was conducted. Consequently, where offshore grid points were located close to the coastline, low *MMI* shaking was assigned to a small number of onshore pixels (Fig. 8). This significantly reduced modelled landslide hazard in the corresponding pixels and thus road blockage risk values for coastal segments of SH1. The small

total area affected by these anomalies explains why the landslide model remains comparable to Model 1 in terms of overall landslide occurrence. Likewise, the lack of order 3+ rivers in these locations explains why the model also remains comparable to Model 1 in terms of landslide dam risk. Had offshore points been removed from the interpolation process at the time of the modelling campaign, the resulting shaking raster would not have included anomalously low *MMI* values onshore along the coast, resulting in the successful prediction of road blockages on coastal SH1. Re-processing Model 2 using the corrected shaking data confirms this (Fig. 8). This emphasises the importance of the initial input data and its handling, with errors and anomalies in the data itself or in the data processing carrying through to final outputs, affecting the overall model success.

Implications for near real-time earthquake impact modelling

We have shown that near real-time prediction of coseismic landsliding impacts can be successfully and rapidly undertaken following a large earthquake. Currently, several near real-time earthquake loss models exist, including the USGS Prompt Assessment of Global Earthquakes for Response (PAGER; Jaiswal et al., 2011, 2009; Wald et al., 2008) and QLARM (Trendafiloski et al., 2011); however, these models currently do not disaggregate losses by cause. Coseismic landslides can account for large numbers of total earthquake fatalities (Yin et al., 2009; Evans & Bent, 2004; Keefer, 1984) and are the primary cause of damage to linear infrastructure such as transport and utilities networks during earthquakes (Bird & Bommer, 2004). Specifically identifying the impacts resulting from coseismic landslides is therefore important for informing emergency response, as this may enable greater understanding of the causes of impacts at different locations throughout the affected area.

This is particularly highlighted in the assessment of landslide dam risk. Because landslide dams typically form in steep narrow catchments they are often difficult to identify from the ground or from remotely sensed imagery, and so may go unnoticed in the immediate aftermath of a large earthquake. The majority of landslide dams that fail do so soon after they form (Costa & Schuster, 1988). Rapidly identifying the locations where landslide dams have formed is therefore vital for post-earthquake response. However, current manual mapping techniques relying on optical aerial and/or satellite reconnaissance are unsuitable for such a task because they can be slow and weather dependent. Initial, incomplete landslide inventories identified from satellite imagery only became available > 5 days after the Kaikōura earthquake had occurred (Sotiris et al., 2016). However, this initial inventory contained < 10% of the total landslides mapped by Massey et al. (This Issue), while an updated inventory released > 12 days after the earthquake still only contained ~ 50%. Further, identification of landslide dams was not completed until 18 days after the earthquake. In contrast, Model 1 was successfully completed < 24 hours after the earthquake, with Model 2 available ~ 72 hours after the earthquake. Effective near real-time modelling of landsliding and associated losses can clearly provide a faster assessment of post-earthquake risk from hazards such as landslide dams. Using these outputs to prioritise locations for aerial and satellite reconnaissance is therefore likely to provide a better approach to rapidly identifying coseismic landslide impacts.

Model use in response to the Kaikōura earthquake

Upon completion, the near real-time model outputs (Figs. 4 & 5) were shared with the earthquake response SAG and uploaded to the clearinghouse. The SAG met regularly during the response via video conference to discuss the evolving situation and consider new information as it became available. The landslide model outputs were initially uploaded to the clearinghouse for

discussion within the SAG to formulate a useful and consistent interpretation of the results that could be shared with relevant stakeholders.

At the time, the model outputs proved useful in two primary ways. Firstly, Model 1 results were shared with the NZTA on 15 November UTC in order to help inform their strategy meeting that day. Of particular interest was the landslide dam risk as, > 48 hours after the earthquake, the road functionality was generally known to NZTA. However, NZTA remained concerned about the threat of outburst floods to key bridges as well as to engineering teams tasked with attempting to reinstate the roads. A further concern was identifying how many people were inaccessible by road and at risk of outburst flood in order to inform decisions of potential emergency evacuation.

Secondly, several members of the SAG were involved in aerial reconnaissance of the affected area, with a particular focus on identifying and monitoring landslide dams. The results of both Model 1 and Model 2 were therefore used to prioritise flight paths over the affected region. As a result, reconnaissance flights between 15 and 23 November undertook flight paths that focussed on the small catchments between the epicentral region and the hills immediately north of Kaikōura, where the majority of landslide dams were predicted and later identified. While this area was considered high priority prior to the model results becoming available, the models did enable more detailed prioritisation of individual catchments.

Future automation

Once a decision to manually apply the coseismic landslide impact model had been taken, the majority of the time required to produce the initial model outputs comprised downloading and processing the required data. This time could be substantially reduced by creating a standing repository of the necessary model data. The only input data not available pre-earthquake are the

599 resulting shaking data and thus the majority of the data can be acquired and consequent
600 calculations undertaken before an earthquake occurs (Fig. 2). Manual application of the model
601 took ~ 31 mins from the completion of data download and preparation. With initial shaking data
602 available from the USGS < 10 mins after an earthquake, Model 1 predictions could therefore
603 have been available within 45 mins of the Kaikōura earthquake occurring, under ideal
604 circumstances.

605 Ideally, this time could further be reduced by automating the method so that manual
606 intervention is not required. This would allow the model to produce results consistently
607 regardless of time of day, week, or year. The relative simplicity of the approach and underlying
608 calculations makes automation of this method a simple task, especially since most of the
609 calculations can be undertaken *a priori*. Furthermore, presently, the model violates a primary
610 condition of near real-time modelling systems in that it is reliant on external calculations of
611 shaking intensity. The model therefore needs to be adapted to be entirely independent by
612 incorporating its own internal shaking intensity estimates. Alternatively, specifically developing
613 the method as an add-on to current near real-time shaking predictions, such as the USGS
614 ShakeMap or PAGER, would allow it to use the resulting shake maps directly, effectively
615 incorporating it into these existing near real-time models and further reducing the time required.
616 Under such conditions, landslide impact predictions could be completed within 10-15 mins of the
617 earthquake occurring, at the same time as the first shaking models become available.

618 **Limitations and uncertainties**

619 Despite the modelling presented having been shown to be useful for a post-earthquake
620 emergency response, there are important limitations to consider. Most importantly, the landslide
621 hazard models (Figs. 4b and 5b), and to a lesser degree the landslide dam models (Figs. 4d and

622 5d), are significantly over-predicted. This is a major limitation of the model and makes the
623 output, in its current form, ineffective at pinpointing the precise locations of landslides caused by
624 the earthquake. However, as highlighted above, these RTP rates are likely minimum values due
625 to the landslide inventory used in verification comprising point sources rather than polygons.
626 Reassessing the RTP rates when polygon source become available will allow the true RTP rate to
627 be calculated allowing a fairer estimation of the true over-prediction. Nevertheless, the model
628 outputs are still expected to be over-predicted and this must be addressed in future iterations if
629 this technique is to prove useful in an emergency response.

630 The models outputs do not presently take the form of a binary prediction of landslide
631 occurrence, but instead are presented as a continuous scale of landslide hazard or risk (i.e.
632 relative likelihood of landslide occurrence). While such a continuous output may have some
633 benefits, the outputs would arguably be enhanced for response purposes by converting to a direct
634 prediction of where landslides have occurred. The limitation here is determining which threshold
635 value to set in order to form a binary prediction, which is ultimately subjective, and the utility to
636 end-users of true probability values. A recent attempt has been made to model landslide hazard
637 in terms of true probability, using observations from relatively large numbers of global
638 earthquakes (Parker et al., 2017). While this approach has been shown to yield consistently
639 accurate predictions of landslide probability from test earthquakes, it has yet to be applied in
640 (near) real-time following an earthquake.

641 The model outputs provide no information on the potential size, mechanism, or
642 consequent damage of the landslides triggered. At a local scale, the total volume and area
643 involved in a landslide, as well as the mechanism and style of motion, are vital indicators of the
644 hazard posed, and the potential damage. Vulnerability of roads to landslide losses is also a

645 critical component of risk. Currently the model only assesses the likelihood of landslides
646 reaching the road network, not the damage that they cause. Similarly, for landslide dams, the
647 model currently only predicts the likelihood of a landslide reaching the river; it does not consider
648 the potential for the landslide to subsequently block the river, which may further explain the
649 over-prediction in this component of the model. Finding ways to incorporate such information
650 into future models could therefore improve the overall usefulness and further reduce over-
651 prediction.

652 Finally, this is the only time that this method has been attempted during a live earthquake
653 response. Whilst the results are encouraging, particularly for road blockage prediction, and the
654 use of the outputs highlights the need for and value of such models, it is not guaranteed that
655 applying the same model to future earthquakes elsewhere will produce similarly successful
656 results. Consequently, further testing of the method on historic earthquakes is required before it
657 can be more widely operationalised. Despite this, the underlying hazard model of Kritikos et al.
658 (2015) has now been shown to be successful for three different earthquakes in New Zealand, and
659 thus New Zealand seems likely to prove a suitable site for continued testing and initial
660 implementation of this near real-time modelling approach.

661 **CONCLUSIONS**

662 Following the 13 November 2016 UTC Kaikōura earthquake in New Zealand, we undertook a
663 near real-time landslide hazard and impact modelling campaign in an attempt to provide critical
664 information for emergency responders. The landslide hazard model used an empirical approach
665 using fuzzy logic in GIS based on global observations of the relationships between landslide
666 occurrence and predisposing factors. The impact models used a simplified analysis of landslide

mobility based on reach angles to identify pixels from which any landslide posed a risk to nearby roads and rivers. The model did not account for vulnerability of roads and rivers to landslide blockage, instead focussing simply on locations where landslides could intersect the feature. The approach was undertaken manually following the earthquake and therefore its capabilities as an automatic system have not been properly tested.

The outputs from these models accurately accounted for the majority of landslides, road blockages and landslide dams that formed during the earthquake. Importantly, the first models, based on initial shaking outputs from the USGS, were available just 21 hrs 28 mins after the earthquake, > 4 days before the first, incomplete assessment of landsliding from traditional mapping efforts. A second iteration of the model based on updated shaking outputs was available ~72 hrs after the earthquake and generally performed better than the initial model. While both models accurately accounted for the majority of landslides and landslide dams, it is notable that these models were especially over-predicted, and therefore require continued refinement to the modelling methods to reduce this over-prediction. Nevertheless, the model was able to perform well in identifying road blockages, with limited over-prediction observed suggesting this approach may prove useful at accurately predicting road impacts from landslides in future earthquakes.

While the present results are promising, continued efforts to streamline and automate the modelling methods is required. An automated version of the model may be able to produce future outputs within 10-15 mins of an earthquake occurring, significantly improving the times achieved in this study through manual application. Incorporating the vulnerability of roads and rivers into the model is a further aim, as this is a crucial component of any disaster management system as its assessment can be used as an input for decision making during an emergency

response. Finally, efforts to improve the model in order to reduce the over-prediction associated with the landslide hazard and landslide dam risk outputs is essential if future iterations are to be useful for pinpointing the precise locations of landslides and landslide dams.

DATA & RESOURCES

Landslide and road blockage data used in this study were collected from the private *Engineering Response to the M7.8 Kaikoura earthquake clearinghouse* set up for secure data sharing post-earthquake and is not available to the public. The landslide inventory used in this study to assess model performance was kindly supplied to the authors by Chris Massey of GNS Science and is described in Massey et al (This Issue). Publically available data on landslide locations is available from Sotiris et al. (2016) and can be obtained from https://zenodo.org/record/167130#.WZRwt1WGNhG (last accessed August 2017). Landslide dam locations were taken from the Environment Canterbury website and can be accessed at http://ecan.maps.arcgis.com/apps/Cascade/index.html?appid=50f00d42e29c46b1a61b848440c5295a (last accessed August 2017). Shaking data was downloaded at the time from the USGS and GeoNet, and is available from https://earthquake.usgs.gov/earthquakes/eventpage/us1000778i#executive (last accessed November 2016) and http://shakemap.geonet.org.nz/data/2016p858000/output/grid.xml (last accessed Novemeber 2016). All other data in this paper came from published sources listed in the references.

ACKNOWLEDGEMENTS

The authors would like the thank the members of the New Zealand earthquake response SAG who used the outputs of this study at the time and subsequently helped to improve both the model outputs and this manuscript. In particular we thank Liam Wotherspoon for his helpful thoughts and comments which helped improve the manuscript from its original draft, and Chris Massey for providing access to the GNS Science landslide inventory. We thank the two anonymous reviewers whose comments helped improve this manuscript. This study was supported by the DIFeREns2 (2014-2019) COFUND scheme supported by the European Union's Seventh Framework Programme (grant number 609412).

REFERENCES

Bannister, S. & Gledhill, K. (2012). Evolution of the 2010-2012 Canterbury earthquake sequence. *New Zealand Journal of Geology and Geophysics*. 55 (3). p.pp. 295–304.

Bird, J.F. & Bommer, J.J. (2004). Earthquake losses due to ground failure. *Engineering Geology*. 75 (2). p.pp. 147–179.

Borella, J.W., Quigley, M. & Vick, L. (2016). Anthropocene rockfalls travel farther than prehistoric predecessors. *Science Advances*. 2 (9).

Bui, D.T., Pradhan, B., Lofman, O., Revhaug, I. & Dick, O.B. (2012). Spatial prediction of landslide hazards in Hoa Binh province (Vietnam): A comparative assessment of the efficacy of evidential belief functions and fuzzy logic models. *CATENA*. 96. p.pp. 28–40.

Costa, J.E. & Schuster, R.L. (1988). The formation and failure of natural dams. *Geological Soceity of America Bulletin*. 100. p.pp. 1054–1068.

Davies, A.J., Sadashiva, V., Aghababaei, M., Barnhill, D., Costello, S.B., Fanslow, B., Headifen,

731 D., Hughes, M., Kotze, R., Mackie, J., Ranjitkar, P., Thompson, J., Troitino, D.R., Wilson,
732 T., Woods, S. & Wotherspoon, L.M. (2017). Transport infrastructure performance and
733 management in the South Island of New Zealand, during the first 100 days following the 2016
734 Mw 7.8 Kaikōura earthquake. *Bulletin of the New Zealand Society for Earthquake*
735 *Engineering*. 50 (2).
736 Davies, T.R., McSaveney, M.J. & Hodgson, K.A. (1999). A fragmentation-spreading model for
737 long-runout rock avalanches. *Canadian Geotechnical Journal*. 36 (6). p.pp. 1096–1110.
738 Dellow, S., Massey, C., Cox, S., Archibald, G., Begg, J., Bruce, Z., Carey, J., Davidson, J., Pasqua,
739 F. Della, Glassey, P., Hill, M., Jones, K., Lyndsell, B., Lukovic, B., Mccoll, S., Rattenbury,
740 M., Read, S., Rosser, B., Singeisen, C., Townsend, D., Villamor, P., Villeneuve, M.,
741 Wartman, J., Rathje, E., Sitar, N., Adda, A.-Z., Manousakis, J. & Little, M. (2017). Landslides
742 caused by the Mw7.8 Kaikōura earthquake and the immediate response. *Bulletin of the New*
743 *Zealand Society for Earthquake Engineering*. 50 (2).
744 Evans, S.G. & Bent, A.L. (2004). The Las Colinas landslide, Santa Tecla - A highly destructive
745 flowslide triggered by the January 13, 2001, El Salvador earthquake. In: W. I. Rose, J. J.
746 Bommer, D. L. Lopez, M. J. Carr, & J. J. Major (eds.). *Natural Hazards in El Salvador:*
747 *Geological Society of America Special Paper 375*. pp. 25–38.
748 Gallen, S.F., Clark, M.K., Godt, J.W., Roback, K. & Niemi, N.A. (2016). Application and
749 evaluation of a rapid response earthquake-triggered landslide model to the 25 April 2015 Mw
750 7.8 Gorkha earthquake, Nepal. *Tectonophysics*.
751 Giovinazzi, S., Wilson, T., Davis, C., Bristow, D., Gallagher, M., Schofield, A., Villemure, M.,
752 Eidinger, J. & Tang, A. (2011). Lifelines performance and management following the 22
753 February 2011 Christchurch earthquake, New Zealand: Highlights of resilience. *Bulletin of*

754 *the New Zealand Soceity for Earthquake Engineering*. 44 (4). p.pp. 402–417.
755 Godt, J.W., Baum, R.L., Savage, W.Z., Salciarini, D., Schulz, W. & Harp, E.L. (2008). Transient
756 deterministic shallow landslide modelling: requirements for susceptibility and hazard
757 assessments in a GIS framework. *Engineering Geology*. 102. p.pp. 214–226.
758 Hamling, I.J., Hreinsdóttir, S., Clark, K., Elliott, J., Liang, C., Fielding, E., Litchfield, N.,
759 Villamor, P., Wallace, L., Wright, T.J., D'Anastasio, E., Bannister, S., Burbidge, D., Denys,
760 P., Gentle, P., Howarth, J., Mueller, C., Palmer, N., Pearson, C., Power, W., Barnes, P.,
761 Barrell, D.J.A., Van Dissen, R., Langridge, R., Little, T., Nicol, A., Pettinga, J., Rowland, J.
762 & Stirling, M. (2017). Complex multifault rupture during the 2016 Mw 7.8 Kaikōura
763 earthquake, New Zealand. *Science*. eaam7194.
764 Horspool, N.A., Chadwick, M., Ristau, J., Salichon, J. & Gerstenberger, M.C. (2015).
765 ShakeMapNZ: Informing post-event decision making. *Proceedings of the New Zealand*
766 *Society for Earthquake Engineering Conference*.
767 Hsü, K.J. (1975). Catastrophic Debris Streams (Sturzstroms) Generated by Rockfalls. *Geological*
768 *Soceity of America Bulletin*. 86. p.pp. 129–140.
769 Hungr, O. (1995). A model for the runout analysis of rapid flow slides, debris flows, and
770 avalanches. *Canadian Geotechnical Journal*. 32 (4). p.pp. 610–623.
771 Hungr, O. (2006). Rock avalanche occurrence, process and modelling. In: *Landslides from*
772 *Massive Rock Slope Failure*. Dordrecht: Springer Netherlands, pp. 243–266.
773 Jaiswal, K., Wald, D.J., Earle, P.S., Porter, K.A. & Hearne, M. (2011). Earthquake Casualty
774 Models Within the USGS Prompt Assessment of Global Earthquakes for Response (PAGER)
775 System. In: R. Spence (ed.). *Human Casualties in Earthquakes*. Advances in Natural and
776 Technological Hazards Research. 2011.

777 Jaiswal, K., Wald, D.J. & Hearne, M. (2009). *Estimating Casualties for Large Earthquakes*
778 *Worldwide Using an Empirical Approach*.
779 Jibson, R.W., Harp, E.L. & Michael, J.A. (2000). A method for producing digital probabilistic
780 seismic landslide hazard maps. *Engineering Geology*. 58. p.pp. 271–289.
781 Kaiser, A., Balfour, N., Fry, B., Holden, C., Litchfield, N., Gerstenberger, M., D'Anastasio, E.,
782 Horspool, N., McVerry, G., Ristau, J., Bannister, S., Christophersen, A., Clark, K., Power,
783 W., Rhoades, D., Massey, C., Hamling, I., Wallace, L., Mountjoy, J., Kaneko, Y., Benites,
784 R., Van Houtte, C., Dellow, S., Wotherspoon, L., Elwood, K. & Gledhill, K. (2017). The
785 2016 Kaikōura, New Zealand, Earthquake: Preliminary Seismological Report. *Seismological*
786 *Research Letters*. 88 (3).
787 Kanungo, D.P., Arora, M.K., Gupta, R.P. & Sarkar, S. (2008). Landslide risk assessment using
788 concepts of danger pixels and fuzzy set theory in Darjeeling Himalayas. *Landslides*. 5 (4).
789 p.pp. 407–416.
790 Keefer, D.K. (1984). Landslides caused by earthquakes. *Geological Soceity of America Bulletin*.
791 95. p.pp. 406–421.
792 Kritikos, T. & Davies, T. (2015). Assessment of rainfall-generated shallow landslide/debris-flow
793 susceptibility and runout using a GIS-based approach: application to western Southern Alps
794 of New Zealand. *Landslides*. 12 (6). p.pp. 1051–1075.
795 Kritikos, T., Robinson, T.R. & Davies, T.R.H. (2015). Regional coseismic landslide hazard
796 assessment without historical landslide inventories: A new approach. *Journal of Geophysical*
797 *Research : Earth Surface*. 120. p.pp. 1–19.
798 Legros, F. (2002). The mobility of long-runout landslides. *Engineering Geology*. 63 (3–4). p.pp.
799 301–331.

800 Marc, O., Hovius, N. & Meunier, P. (2016). The mass balance of earthquakes and earthquake
801 sequences. *Geophysical Research Letters*. 43 (8). p.pp. 3708–3716.
802 Meinhardt, M., Fink, M. & Tünschel, H. (2015). Landslide susceptibility analysis in central
803 Vietnam based on an incomplete landslide inventory: Comparison of a new method to
804 calculate weighting factors by means of bivariate statistics. *Geomorphology*. 234. p.pp. 80–
805 97.
806 Newmark, N.M. (1965). Effects of earthquakes on dams and embankments. *Milestones in Soil*
807 *Mechanics*.
808 Nowicki, M.A., Wald, D.J., Hamburger, M.W., Hearne, M. & Thompson, E.M. (2014).
809 Development of a globally applicable model for near real-time prediction of seismically
810 induced landslides. *Engineering Geology*. 173. p.pp. 54–65.
811 Parker, R.N., Rosser, N.J. & Hales, T.C. (2017). Spatial prediction of earthquake-induced landslide
812 probability. *Natural Hazards and Earth System Sciences Discussions*.
813 Paterson, B.R. & Bourne-Webb, P.J. (1994). Reconnaissance report on highway damage from the
814 18 June 1994, Arthurs Pass earthquake. *Bulletin of the New Zealand Society for Earthquake*
815 *Engineering*. 27 (3). p.pp. 222–226.
816 Pellicani, R., Van Westen, C.J. & Spilotro, G. (2014). Assessing landslide exposure in areas with
817 limited landslide information. *Landslides*. 11 (3). p.pp. 463–480.
818 Pourghasemi, H.R., Pradhan, B. & Gokceoglu, C. (2012). Application of fuzzy logic and analytical
819 hierarchy process (AHP) to landslide susceptibility mapping at Haraz watershed, Iran.
820 *Natural Hazards*. 63 (2). p.pp. 965–996.
821 Power, W., Downes, G., McSaveney, M., Beavan, J. & Hancox, G.T. (2005). The Fiordland
822 earthquake and tsunami, New Zealand, 21 August 2003. In: K. Satake (ed.). *Tsunamis: Case*

Studies and Recent Developments. 2005, pp. 31–42.

Pradhan, B. (2010). Landslide susceptibility mapping of a catchment area using frequency ratio, fuzzy logic and multivariate logistic regression approaches. *Journal of the Indian Society of Remote Sensing*. 38 (2). p.pp. 301–320.

Robinson, T.R., Buxton, R., Wilson, T.M., Cousins, J. & Christophersen, A. (2015). *Multiple infrastructure failures and restoration estimates from an Alpine Fault earthquake: Capturing modelling information for MERIT*.

Robinson, T.R., Davies, T.R.H., Wilson, T.M. & Orchiston, C. (2016a). Coseismic landsliding estimates for an Alpine Fault earthquake and the consequences for erosion of the Southern Alps, New Zealand. *Geomorphology*. 263. p.pp. 71–86.

Robinson, T.R., Davies, T.R.H., Wilson, T.M., Orchiston, C. & Barth, N. (2016b). Evaluation of coseismic landslide hazard on the proposed Haast-Hollyford Highway, South Island, New Zealand. *Georisk: Assessment and Management of Risk for Engineered Systems and Geohazards*. 10 (2).

Robinson, T.R., Rosser, N.J., Densmore, A.L., Williams, J.G., Kincey, M.E., Benjamin, J. & Bell, H.J.A. (2017). Rapid post-earthquake modelling of coseismic landslide magnitude and distribution for emergency response decision support. *Natural Hazards and Earth Systems Sciences*.

Sotiris, V., George, P. & Spyros, P. (2016). *Preliminary Map of Co-Seismic Landslides for the M 7.8 Kaikoura, New Zealand Earthquake [Data Set]*. 2016. Zenodo.

Stirling, M.W., Litchfield, N.J., Villamor, P., Van Dissen, R.J., Nicol, A., Pettinga, J., Barnes, P., Langridge, R.M., Little, T., Barrell, D.J.A., Mountjoy, J., Ries, W.F., Rowland, J., Fenton, C., Hamling, I., Asher, C., Barrier, A., Benson, A., Bischoff, A., Borella, J., Carne, R.,

846 Cochran, U.A., Cockroft, M., Cox, S.C., Duke, G., Fenton, F., Gasston, C., Grimshaw, C.,
847 Hale, D., Hall, B., Hao, K.X., Hatem, A., Hemphill-Haley, M., Heron, D.W., Howarth, J.,
848 Juniper, Z., Kane, T., Kearse, J., Khajavi, N., Lamarche, G., Lawson, S., Lukovic, B.,
849 Madugo, C., Mccoll, S., Noble, D., Pedley, K., Sauer, K., Stahl, T., Strong, D.T., Townsend,
850 D.B., Toy, V., Villeneuve, M., Wandres, A., Williams, J., Woelz, S. & Zinke, R. (2017). The
851 Mw 7.8 2016 Kaikōura earthquake: surface fault rupture and seismic hazard context. *Bulletin*
852 *of the New Zealand Society for Earthquake Engineering*. 50 (2).
853 Trendafiloski, G., Wyss, M. & Rosset, P. (2011). Loss Estimation Module in the Second
854 Generation Software QLARM. In: R. Spence (ed.). *Human Casualties in Earthquakes*.
855 Advances in Natural and Technological Hazards Research. 2011.
856 Wadge, G., Francis, P.W. & Ramirez, C.F. (1995). The Socompa collapse and avalanche event.
857 *Journal of Volcanology and Geothermal Research*. 66. p.pp. 309–336.
858 Wald, D., Lin, K.-W., Porter, K. & Turner, L. (2008). ShakeCast: Automating and Improving the
859 Use of ShakeMap for Post-Earthquake Decision-Making and Response. *Earthquake Spectra*.
860 24 (2). p.pp. 533–553.
861 Williams, J.G., Rosser, N.J., Kincey, M.E., Benjamin, J., Oven, K.J., Densmore, A.L., Milledge,
862 D.G. & Robinson, T.R. (2017). Satellite-based emergency mapping: Landslides triggered by
863 the 2015 Nepal earthquake. *Natural Hazards and Earth System Sciences Discussion*.
864 Woods, R.J., McBride, S.K., Wotherspoon, L.M., Beaven, S., Potter, S.H., Johnston, D.M.,
865 Wilson, T.M., Brunsdon, D., Grace, E.S. & Brackley, H. (2017). Science to Emergency
866 Management Response: Kaikoura Earthquakes 2016. *Bulletin of the New Zealand Soceity for*
867 *Earthquake Engineering*. 50 (2). p.pp. 329–337.
868 Yin, Y., Wang, F. & Sun, P. (2009). Landslide hazards triggered by the 2008 Wenchuan

869 earthquake, Sichuan, China. *Landslides*. 6 (2). p.pp. 139–152.

870

LIST OF FIGURES:

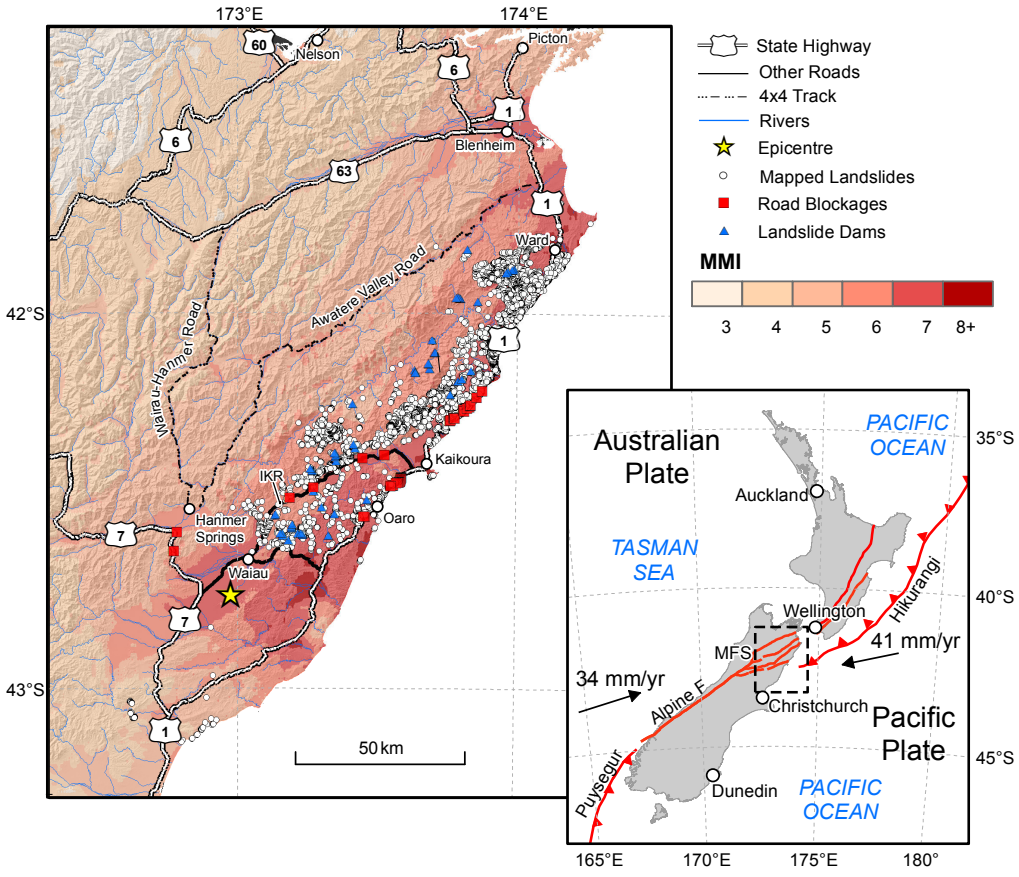

Figure 1: Ground shaking and observed landslides from the M_w 7.8 Kaikōura earthquake in relation to critical transport infrastructure and rivers. Shaking data from GeoNet downloaded at 10:12 hrs on 16 November 2016 UTC (+2 days 23 hrs 10 mins). Landslides mapped by Massey et al. (This Issue). Landslide road blockages reported by the New Zealand Transport Agency and downloaded from the clearinghouse > 1 week after the event. Landslide dams located by ECan (2017a) based on aerial reconnaissance and publically released on 1 December 2016 UTC (+18 days). Inset: Tectonic setting of New Zealand showing major faults associated with the Australia-Pacific plate boundary. MFS – Marlborough Fault System; Alpine F – Alpine Fault; IKR – Inland Kaikōura Road.

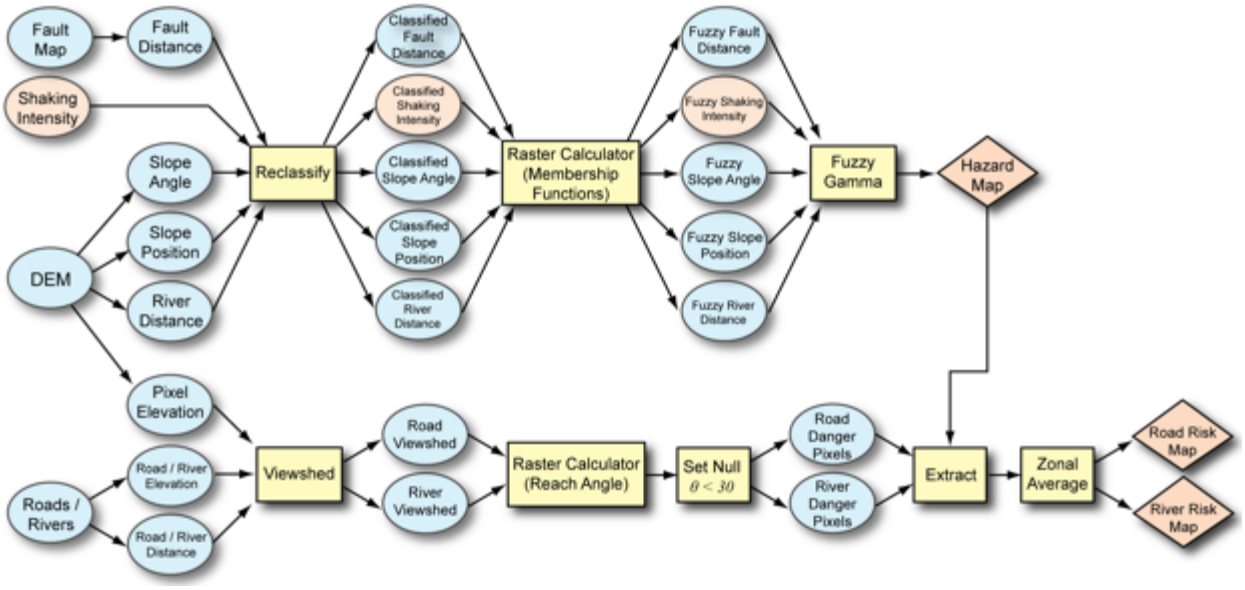

882

883 Figure 2: Simplified workflow for near real-time landslide hazard and risk modelling. Circles
884 represent input or derived data; squares represent model processes; diamonds represent key
885 model outputs. All data except shaking intensity and its consequent derived data is available pre-
886 earthquake.

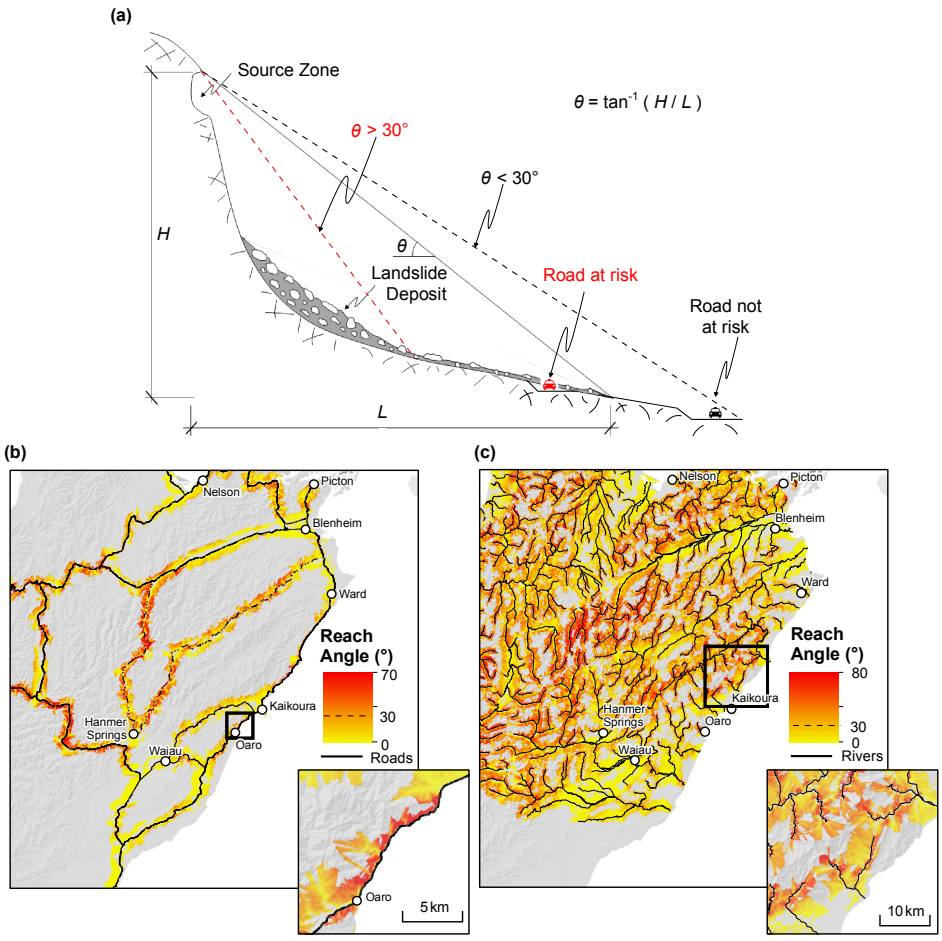

887

888 Figure 3: Landslide reach angle and danger pixels for the South Island State Highway and order
889 3+ river networks. (a) Landslide runout concepts, adapted from Hungr et al. (2005). *H* – vertical
890 drop; *L* – horizontal distance; *θ* – reach angle. Pixels with reach angles > 30º are considered to be
891 at risk from landslide blockages, while pixels with reach angles < 30° are not at risk. (b)
892 Calculated reach angles for all pixels surrounding the road network. Inset: closer view of
893 calculated reach angles for a section of SH1 north of Oaro. (c) Calculated reach angles for all
894 pixels surrounding the order 3+ river network. Inset: closer view of calculated reach angles for
895 series of rivers north of Kaikōura.

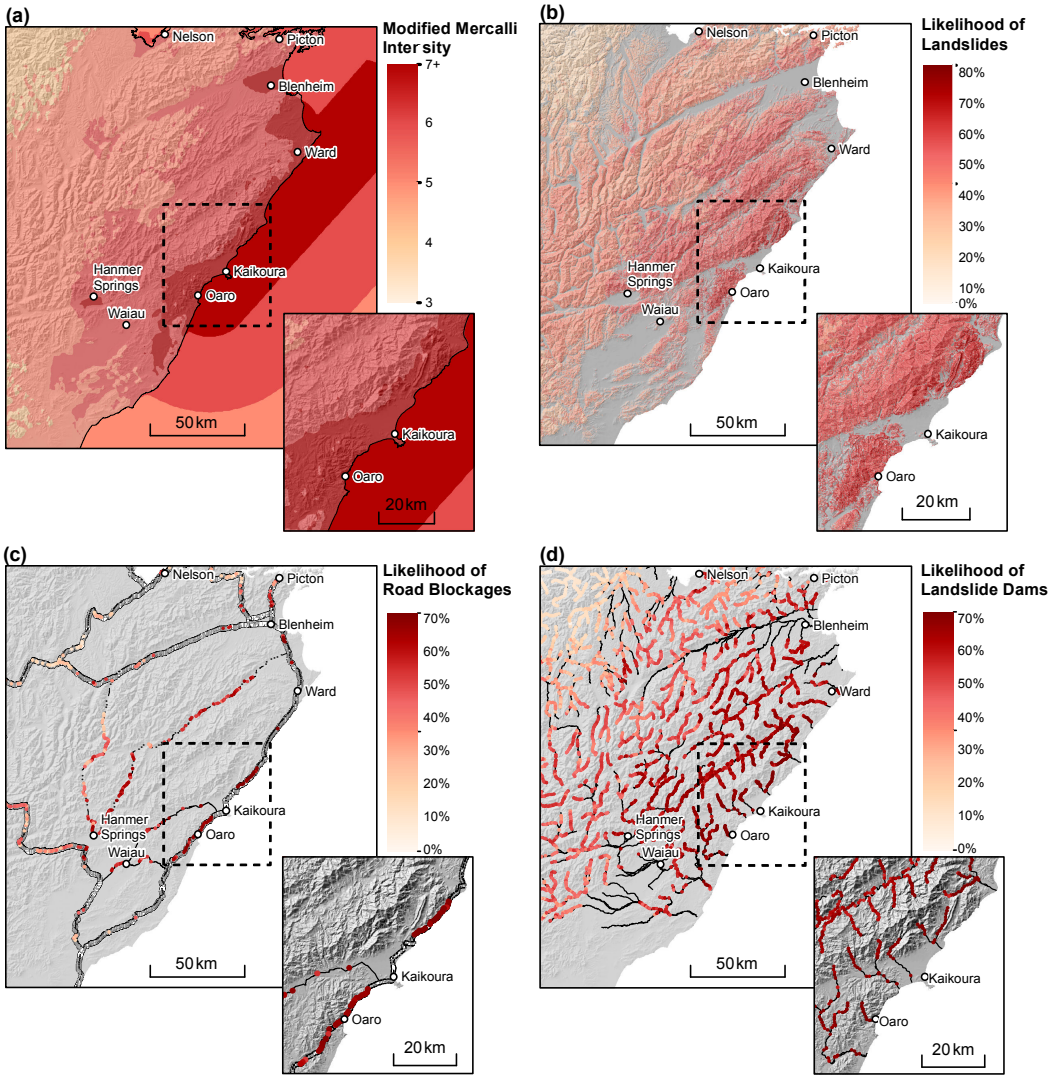

896

897 Figure 4: Model 1 landslide hazard and risk model results based on the USGS ShakeMap®
898 version 1, completed at 08:30 hrs on 14 November UTC (+0 days 21 hrs 28 mins). (a) input
899 ground shaking model from USGS; (b) landslide hazard model; (c) landslide road blockage risk
900 model; (d) landslide dam risk model.

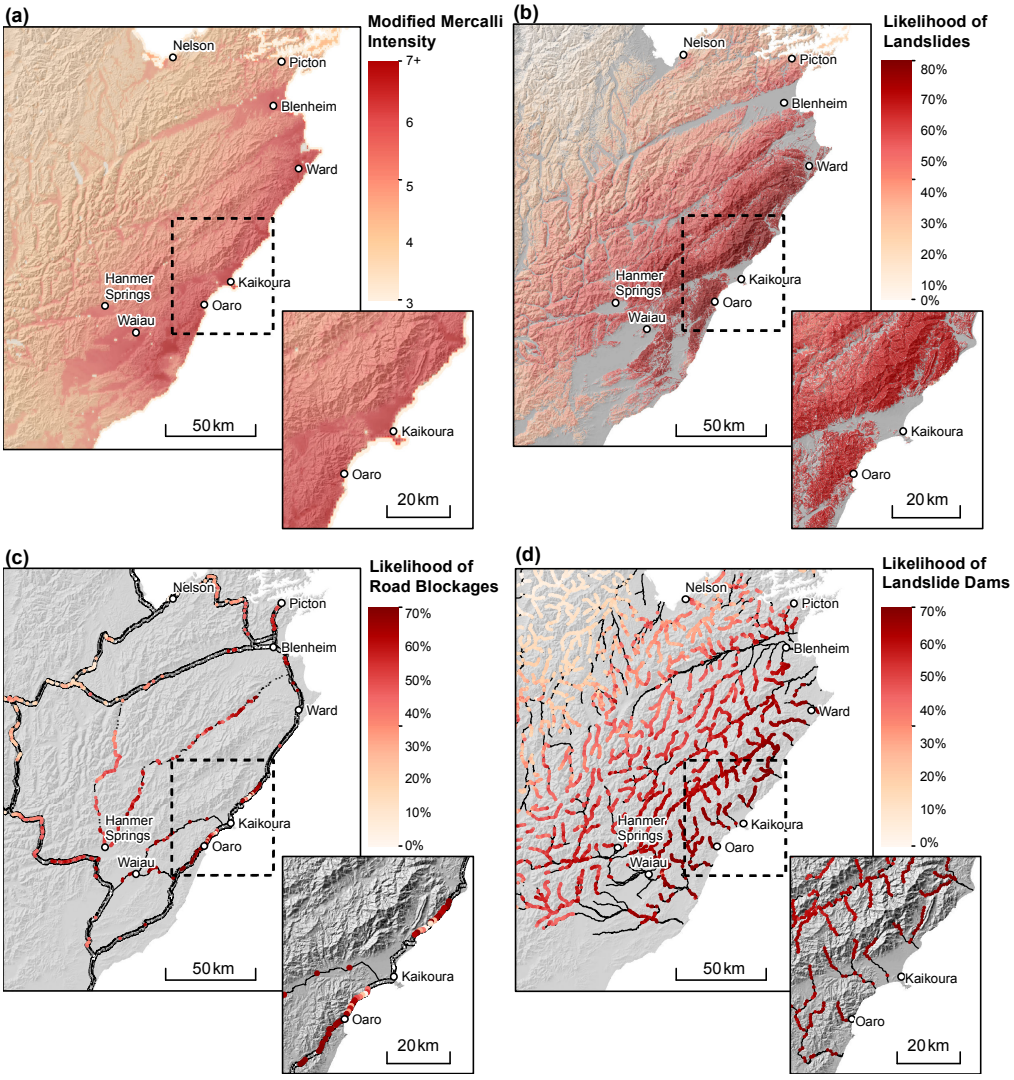

Figure 5: Model 2a landslide hazard and risk model results based on the GeoNet Shakemap version 1, completed at 12:30 hrs on 16 November UTC (+3 days 1 hrs 28 mins). (A) input ground shaking model from GeoNet. The blue halo of low intensity shaking along the entire coastline resulted from an anomaly in the data processing at the time; (B) landslide hazard model; (C) landslide road blockage risk model; (D) landslide dam risk model.

907 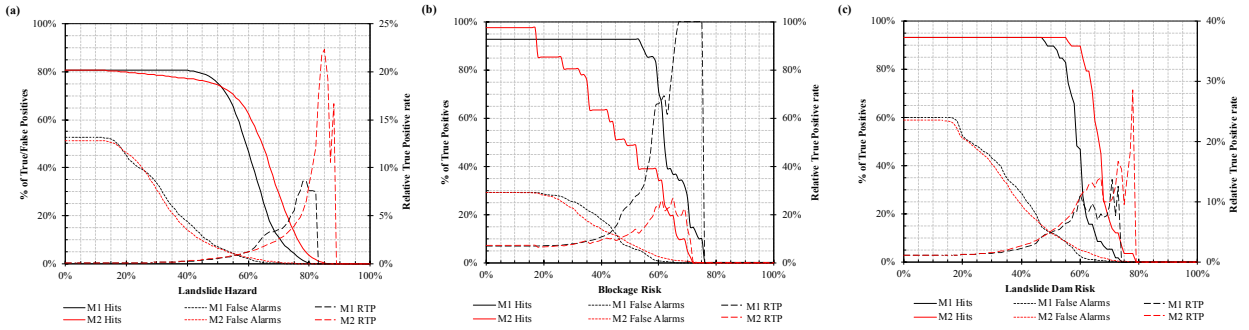

908 Figure 6: Quantitative verification curves showing true positive, false positives, and relative true
909 positive rates for each of the Model 1 and Model 2 outputs based on initial observed landslides.
910 (A) landslide hazard outputs; (B), road blockage risk outputs; (C), and landslide dam risk
911 outputs. True positive curves for road blockages and landslide dams appear step-wise due to the
912 small number of observed blockages used to verify the models.

913 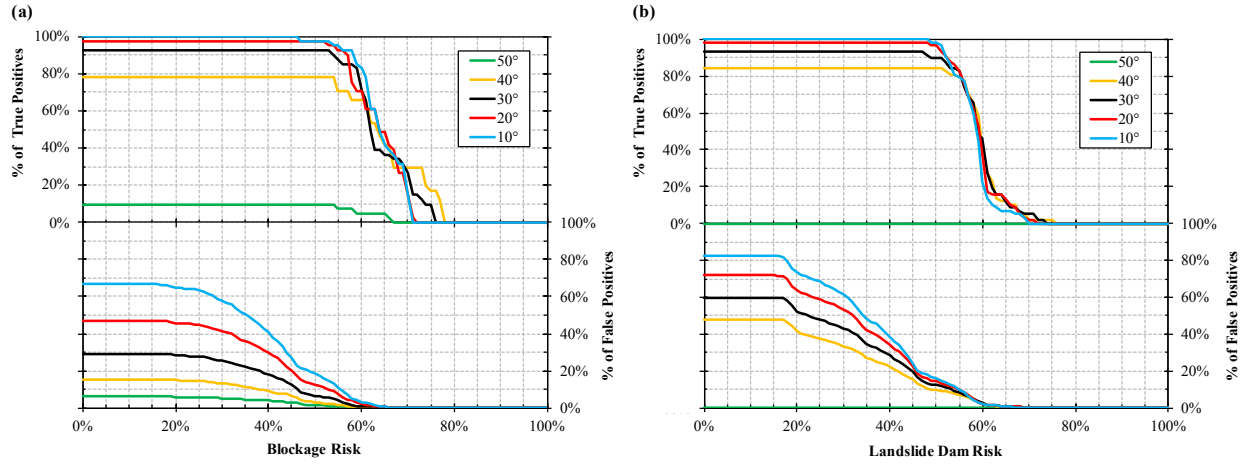

914 Figure 7: Effect of using different reach angle thresholds on the percentage of true positives and
915 false positives predicted by Model 1 for road blockages and landslide dams. (A) True and false
916 positive curves for different reach angle thresholds for road blockage risk; and (B) true and false
917 positive curves for different reach angle thresholds for landslide dam risk. Decreasing the reach
918 angle threshold increases the maximum number of hits successfully predicted, but has an

associated increase in false alarms. The area between the true and false positive curves for the same threshold angle gives a measure of the best performing threshold value.

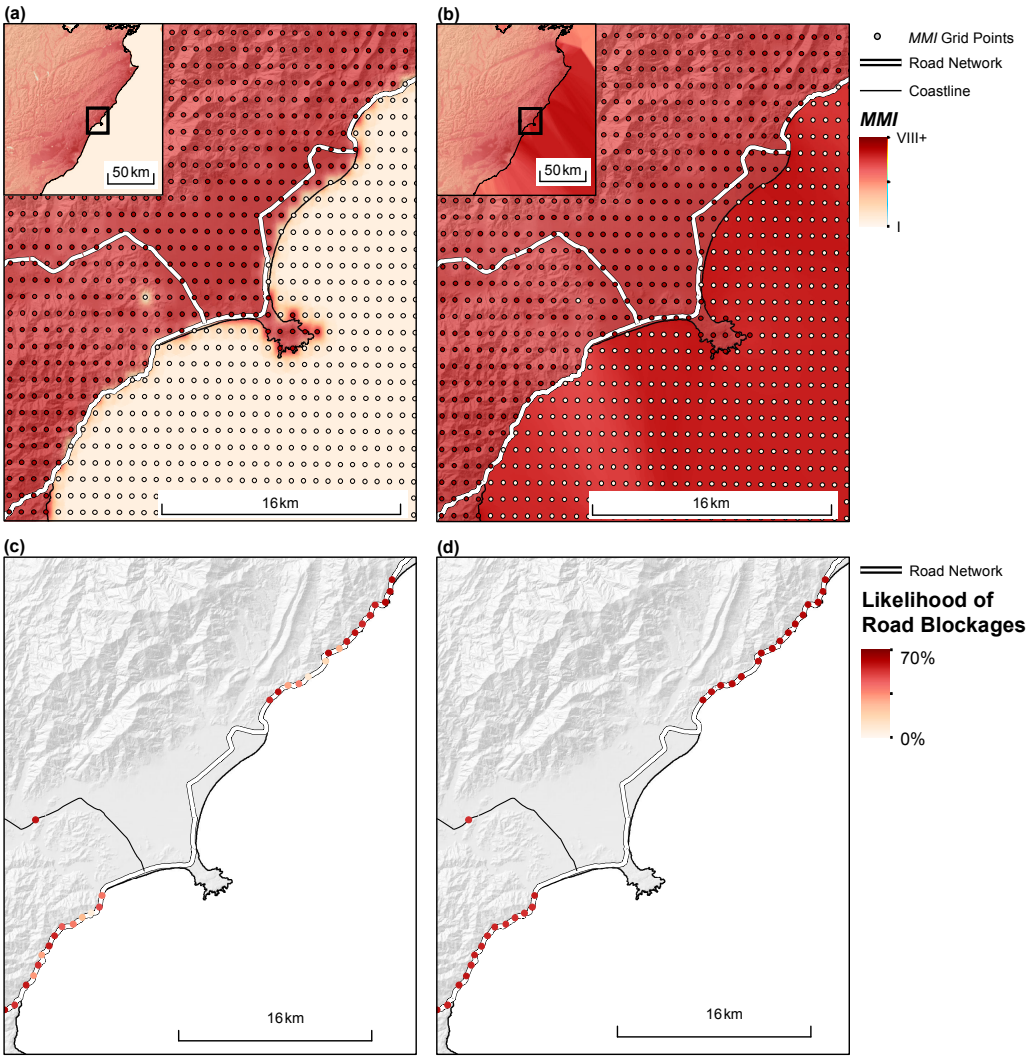

Figure 8: Comparison between *MMI* raster files computed using all grid points in the GeoNet data download and only those grid points located onshore, and the effect on predicted road risk. (A) Interpolated raster file using all grid points; (B) Interpolated raster file using only onshore grid points; (C) Predicted road blockage risk near Kaikōura for Model 2 using *MMI* in (A); and (D) Predicted road blockage risk near Kaikōura for Model 2-corrected using *MMI* in (B).

927 **TABLES**

928 Table 1: Bin ranges and corresponding bin numbers for each of the predisposing factors used in

929 this study.

Factor	Bin value range	Bin number
Local slope angle (*SA*)	0-5º	1
	5-10º	2
	10-15º	3
	15-20º	4
	20-25º	5
	25-30º	6
	30-35º	7
	35-40º	8
	40-45º	9
	45-50º	10
	50º+	11
Modified Mercalli Intensity (*MMI*)	1	1
	2	2
	3	3
	4	4
	5	5
	6	6
	7	7

	8	8
	9	9
	10+	10
Fault proximity (*FD*)	0-5 km	1
	5-10 km	2
	10-20 km	3
	20-30 km	4
	30-40 km	5
	40-50 km	6
	50+ km	7
River Proximity (*RD*)	0-0.5 km	1
	0.5-1.0 km	2
	1.0-1.5 km	3
	1.5-2.0 km	4
	2.0-2.5 km	5
	2.5+ km	6
Slope Position (*SP*)*	Flat	1
	Valley bottoms	2
	Mid-slopes	3
	Ridgelines	4

930 *Slope position is a qualitative measure based on a combination of slope angle, slope curvature, and elevation of
931 neighbouring pixels. The classification in this study follows the example given in Jenness et al. (2013).

932

933 Table 2: Sensitivity analysis for Model 1 road blockage and landslide dam outputs.

	Area between true and false positive curves (/1)	
Reach Angle Threshold	Roads Blockages	Landslide Dams
10°	0.36	0.27
20°	0.42	0.30
30°	0.48	0.32
40°	0.46	0.33
50°	0.03	0.00

934